

# Multiple merging in the Abell cluster 1367.\*

L.Cortese<sup>1</sup>, G.Gavazzi<sup>1</sup>, A.Boselli<sup>2</sup>, J.Iglesias-Paramo<sup>2</sup>, and L.Carrasco<sup>3,4</sup>

<sup>1</sup> Universitá degli Studi di Milano-Bicocca, P.zza della Scienza 3, 20126 Milano, Italy.  
e-mail: Luca.Cortese@mib.infn.it; Giuseppe.Gavazzi@mib.infn.it

<sup>2</sup> Laboratoire d'Astrophysique de Marseille, BP8, Traverse du Siphon, F-13376 Marseille, France.  
e-mail: alessandro.boselli@oamp.fr; jorge.iglesias@oamp.fr

<sup>3</sup> Instituto Nacional de Astrofisica, Optica y Electronica, Apartado Postal 51 C.P. 72000 Puebla, Pue., Mexico.  
e-mail: carrasco@transum.inaoep.mx

<sup>4</sup> Observatorio Astronomico Nacional/UNAM, Ensenada B.C., Mexico.

Received 4 March 2004 — Accepted 4 June 2004

**Abstract.** We present a dynamical analysis of the central  $\sim 1.3$  square degrees of the cluster of galaxies Abell 1367, based on 273 redshift measurements (of which 119 are news). From the analysis of the 146 confirmed cluster members we derive a significantly non-Gaussian velocity distribution, with a mean location  $C_{BI} = 6484 \pm 81 \text{ km s}^{-1}$  and a scale  $S_{BI} = 891 \pm 58 \text{ km s}^{-1}$ . The cluster appears elongated from the North-West to the South-East with two main density peaks associated with two substructures. The North-West subcluster is probably in the early phase of merging into the South-East substructure ( $\sim 0.2$  Gyr before core crossing). A dynamical study of the two subclouds points out the existence of a group of star-forming galaxies infalling into the core of the South-East subcloud and suggests that two other groups are infalling into the NW and SE subclusters respectively. These three subgroups contain a higher fraction of star-forming galaxies than the cluster core, as expected during merging events. Abell 1367 appears as a young cluster currently forming at the intersection of two filaments.

**Key words.** Galaxies: clusters: individual: A1367 - Galaxies: evolution - Galaxies: distances and redshift

## 1. Introduction

Clusters of galaxies represent the most massive gravitationally bound systems in the Universe. They provide us with valuable insights into the formation of large-scale structures, as well as into the formation and evolution of galaxies. The hierarchical model predicts that galaxy clusters are formed by accretion of units of smaller mass at the nodes of large-scale filaments (West et al. 1991; Katz & White 1993). Statistical analyses of clusters have shown that even at low redshift a high fraction of clusters presents substructures, implying that clusters are still dynamically young units, undergoing the process of formation (Dressler & Shectman 1988).

The Abell cluster 1367 ( $z \sim 0.0216$ ) lies at the intersection of two filaments, the first extending roughly 100 Mpc from Abell 1367 toward Virgo (West & Blakeslee 2000), the second connecting Abell 1367 to Coma (as a part of

the Great Wall, Zabludoff et al. 1993). With its irregular X-ray distribution (Jones et al. 1979; Bechtold et al. 1983; Grebenev et al. 1995), high fraction of spiral galaxies and low central galaxy density, Abell 1367 can be considered as the prototype of a nearby dynamically young cluster. ASCA X-ray observations pointed out the existence of a strong localized shock in the intra-cluster medium (ICM) suggesting that Abell 1367 is experiencing a merging between two substructures (Donnelly et al. 1998). Moreover recent Chandra observations (Sun & Murray 2002), and a preliminary analysis of the XMM data (Forman et al. 2003), indicate the presence of cool gas streaming into the cluster core, supporting a multiple merger scenario. Optical and radio observations also suggest that this cluster is currently experiencing galaxy infall into its center. Gavazzi et al. (1995, 2001) discovered two head-tail radio sources associated with disk galaxies with an excess of giant HII regions on their leading edges, in the direction of the cluster center. The observational scenario is consistent with the idea that ram-pressure (Gunn & Gott 1972) is, for a limited amount of time, enhancing the star formation of galaxies that are entering the cluster medium. In addition Gavazzi et al. (2003b) pointed out the existence

*Send offprint requests to:* L.Cortese

\* Based on observations obtained with the William Herschel Telescope operated on the island of La Palma (Spain) by the Isaac Newton Group, with the Loiano telescope belonging to the University of Bologna (Italy) and with the G.Haro telescope of the INAOE (Mexico).

of a group of star bursting galaxies infalling into the cluster core.

Although X-ray, radio and optical observations suggest that Abell 1367 is dynamically young and it is still undergoing the process of formation, detailed spatial and dynamical analysis of this cluster has not been attempted so far. Girardi et al. (1998) detected a secondary peak in the cluster velocity distribution, suggesting that Abell 1367 is a binary cluster, but their analysis was based on  $\sim 90$  redshifts, insufficient for drawing a detailed model of the cluster kinematics.

Cortese et al. (2003) carried out a deep ( $r' < 20.5$ ) spectroscopic survey of the central  $\sim 1.3$  square degrees of Abell 1367 adding 60 new spectra (33 members). Here we present new measurements for 119 galaxies (adding another 33 cluster members). In total 273 redshifts were measured in the region, out of which 146 are cluster members, allowing the first detailed dynamical analysis of Abell 1367.

This paper is arranged as follows: Sec.2 briefly describes the studied sample and it contains a description of the observations and data reduction. The analysis of the 1D velocity distribution is given in Sec.3. Tests of 3D substructure are presented in Sec.4. The various spatial and/or velocity substructures detected in our sample are studied in Sec.5. The star formation of galaxies in the infalling groups is discussed in Sec.6. The mass of the whole cluster and of the two main substructures are computed in Sec.7. Sec.8 studies the current dynamical state of the system. Our conclusions are briefly summarized in Sec.9.

We assume a cluster distance of 91.3 Mpc (Gavazzi et al. 1999) corresponding to a Hubble constant of  $71$   $\text{km s}^{-1} \text{Mpc}^{-1}$ .

## 2. Observations and data reduction

The cluster region analyzed in this work covers an area of  $\sim 1.3$  square degrees centered at  $\alpha(J.2000) = 11h44m00s$   $\delta(J.2000) = 19d43m30s$ .  $r'$  imaging material was used to extract a catalogue of galaxy candidates in Abell 1367 complete to  $r' \sim 20.5$  mag, and to select the targets of the present spectroscopic survey. The majority of the photometric catalogue, covering the northern and western part of Abell 1367, was published by Iglesias-Páramo et al. (2003); conversely the south-east catalogue extension will be given in a forthcoming paper.

Spectroscopy of Abell 1367 was obtained with the AF2-WYFFOS multi fiber spectrograph at the 4.2m William Herschel Telescope (WHT) on La Palma (Spain) during 2003, March 27-29. WYFFOS has 150 science fibers of 1.6 arcsec diameter coupled to a bench-mounted spectrograph which relies on a TEK  $1024 \times 1024$  CCD. The 316R grating was used, giving a dispersion of  $\sim 240$   $\text{\AA}/\text{mm}$ , a resolution of  $\sim 6$   $\text{\AA}$  FWHM, and a total spectral coverage of  $\sim 5600$   $\text{\AA}$ . The spectra were centered at  $\sim 6500$   $\text{\AA}$ , thus covering from  $3600$   $\text{\AA}$  to  $9400$   $\text{\AA}$ . We allocated typically  $\sim 70$  objects to fibers in a given configuration and, on average, 15 sky fibers. A total of 4 configurations were executed, with

an exposure time of  $4 \times 1800$  sec for each configuration. Argon lamps for wavelength calibration were obtained for each exposure.

The reduction of the multi fiber spectra was performed in the IRAF<sup>1</sup> environment, using the IMRED package. After bias subtraction, the apertures were defined on dome flat-field frames and used to trace the spectra on the CCD. The arc spectra were extracted and matched with arc lines to determine the dispersion solution. The rms uncertainty of the wavelength calibration ranged between 0.1 and 0.3  $\text{\AA}$ . The lamps' wavelength calibration was checked against known sky lines. These were found within  $\sim 0.5$   $\text{\AA}$  of their nominal position, providing an estimate of the systematic uncertainty on the derived velocity of  $\sim 25$   $\text{km s}^{-1}$ . The object spectra were extracted, wavelength calibrated and normalized to their intensity in the interval 5400-5600  $\text{\AA}$ . A master sky spectrum, that was constructed by combining various sky spectra was normalized to each individual science spectrum and then subtracted from it. Unfortunately strong sky residuals were left after this procedure, limiting the number of useful spectra to 98 (as listed in Tab. 7).

Nine additional long-slit, low dispersion spectra were obtained in March 2003 and in February 2004 using the imaging spectrograph BFOSC attached to the Cassini 1.5m telescope at Loiano (Italy). Another twelve spectra were taken with LFOSC at the 2.1m telescope of the Guillermo Haro Observatory at Cananea (Mexico). These observations were performed using a 2.0 arcsec slit and the wavelength calibration was secured with exposures of HeAr and XeNe lamps at Loiano and Cananea respectively. The on-target exposure time ranged between 15 and 30 min according to the brightness of the targets. After bias subtraction, when 3 or more frames of the same target were obtained, these were combined (after spatial alignment) using a median filter to help cosmic rays removal. Otherwise the cosmic rays were removed using the task COSMICRAYS and/or under visual inspection. The lamps wavelength calibration was checked against known sky lines. These were found within  $\sim 1$   $\text{\AA}$  from their nominal position, providing an estimate of the systematic uncertainty on the derived velocity of  $\sim 50$   $\text{km s}^{-1}$ . After subtraction of sky background, one-dimensional spectra were extracted from the frames.

The redshift were obtained using the IRAF FXCOR Fourier cross-correlation (Tonry & Davis 1979) task, excluding the regions of the spectra affected by night-sky lines. Moreover all the spectra and their best correlation function were visually examined to check the redshift determination.

Table 1 lists the characteristics of the instrumentation in the adopted set-up.

The 119 new velocity measurements presented in this work

<sup>1</sup> IRAF is distributed by the National Optical Astronomy Observatories, which is operated by the Association of Universities for Research in Astronomy, Inc., under the cooperative agreement with the National Science Foundation

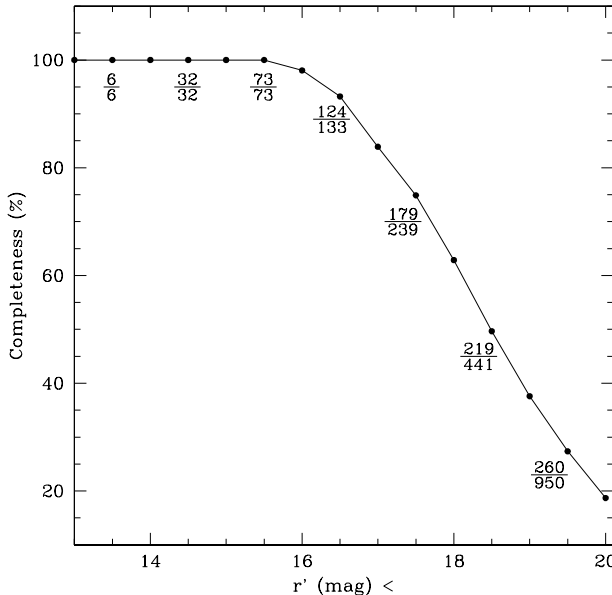


**Fig. 1.** Cumulative redshift distribution for galaxies in the studied region.

are listed in Table 7 as follows:

Column 1: Galaxy designation.

Column 2, 3: (J2000) celestial coordinates, measured with few arcsec uncertainty.

Column 4:  $r'$  band magnitude.

Column 5: observed recessional velocity.

Column 6: telescope (WHT=William Herschel Telescope; LOI=Loiano; CAN=Cananea)

Combining the new set of 119 redshifts (given in Tab. 7) with the ones available from the literature (NED; Cortese et al. 2003; Rines et al. 2003), we have the redshift for 273 galaxies of which 146 are cluster members ( $4000 \text{ km s}^{-1} \leq V \leq 10000 \text{ km s}^{-1}$ ).

The cumulative redshift distribution, in the observed area, as a function of the  $r'$  magnitude is shown in Fig. 1. The completeness is  $\sim 70\%$  at  $r' < 17.5$ , and it drops to  $\sim 45\%$  at  $r' < 18.5$ .

### 3. The global velocity distribution

The line of sight (LOS) velocity distribution for the 146 cluster members is shown in Fig. 2. The mean and standard deviation are known to be efficient estimators of the central location and scale when the underlying population is gaussian. Unfortunately they are not minimum variance estimators when the nature of the observed population is significantly non-Gaussian. The best location and scale estimators must be resistant to the presence of outliers and robust to a broad range of non-Gaussian underlying populations. Thus, following Beers et al. (1990), we consider the biweight estimator as the best estimator of location ( $C_{BI}$ ) and scale ( $S_{BI}$ ) of the cluster velocity distribution. We find a location  $C_{BI} = 6484 \pm 81 \text{ km s}^{-1}$  and a scale  $S_{BI} = 891 \pm 58 \text{ km s}^{-1}$ , in agreement with previous stud-

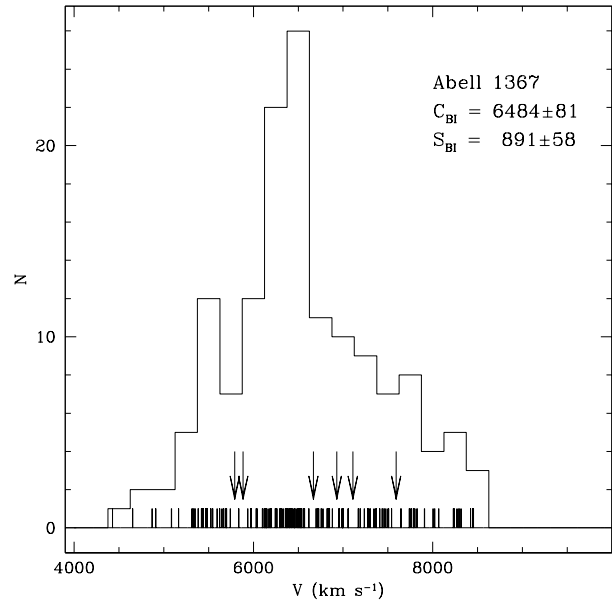


**Fig. 2.** Velocity histogram and stripe density plot for the members of Abell 1367. Arrows mark the location of the most significant weighted gaps in the velocity distribution.

ies (e.g. Girardi et al. 1998; Struble & Rood 1999). Visual inspection of Fig. 2 suggests that the velocity distribution differs from a Gaussian, a deviation that should be quantified using appropriate statistical tests.

We analyze the higher moments of the distributions using the kurtosis and the skewness shape estimators. Kurtosis indicates a difference in the tails length compared to a Gaussian (positive kurtosis is indicative of long tails). Skewness indicates asymmetry (positive skewness implies that the distribution is depleted from values lower than the mean location, conversely negative skewness denotes a depletion of values higher than the mean).

In addition we calculate the asymmetry index (AI) and tail index (TI) introduced by Bird & Beers (1993) as alternatives to the distribution higher moments. These indicators measure the shape of a distribution but, contrary to skewness and kurtosis, which depend on the estimate of the location and the scale of the underlying distribution, they are based on the order statistics of the dataset. The AI measures the symmetry in a population by comparing gaps in the data on the left and right sides of the sample median. The TI compares the spread of the dataset at 90% level to the spread at the 75% level.

The kurtosis, skewness and the TI reject a Gaussian distribution with a confidence level of  $\geq 99\%$ , suggesting that the cluster velocity distribution has longer tails than a Gaussian of the same dispersion. Moreover, in order to assess the normality of the velocity distribution, we use the Wilk - Shapiro (W) test (Yahil & Vidal 1977). Contrary to the  $\chi^2$  and Kolmogorov Smirnov, this test does not require any hypothesis on the mean and variance of the normal distribution. The W test rejects normality with

**Table 1.** The spectrograph characteristics

Observatory	Dates	N. gal.	Spectrograph	Dispersion Å/mm	Coverage Å	CCD	pix μm
WHT	March 03	98	AF2-WYFFOS	240	3600-9400	$1024 \times 1024$ TEK	24
Cananea	March 03	12	LFOSC	228	4000-7100	$576 \times 384$ TH	23
Loiano	March 03 - Feb. 04	9	BFOSC	198	3600-8900	$1340 \times 1300$ EEV	20

**Table 2.** 1D substructure indicators for the whole cluster sample

Test	Value	Rejection of a gaussian
AI	-0.077	$\leq 80$ %
TI	1.240	$>99$ %
Skewness	0.269	$>99$ %
Kurtosis	2.680	$>99$ %
W	0.963	98.7 %

a confidence level of 98.7%, in agreement with kurtosis, skewness and TI (see Table 2).

The departure from a normal distribution could result from a mixture of several velocity distributions with different location and smaller velocity dispersion than the whole sample; thus, using the program ROSTAT (Beers et al. 1990), we investigate the presence of significant gaps (Beers et al. 1991) in the velocity distribution, indicating subclustering. A weighted gap is defined by:

$$y_i = \left( i(N-i) * (x_{i+1} - x_i) \right)^{1/2}$$

where  $N$  is the number of values in the dataset. A weighted gap is significant if its value, relative to the midmean (the mean of the central 50% of the dataset) of the other weighted gaps, is greater than 2.25. This value corresponds to a probability of occurrence in a normal distribution of less than 3%. We detected six significant weighted gaps in the Abell 1367 velocity distribution. The stripe density plot of radial velocities and the position of each gap (indicated with an arrow) are shown in Fig. 2. The velocity of the object preceding each gap, the normalized size of the gap and the probability of finding a normalized gap of the same size and position in a normal distribution are listed in Table 3.

#### 4. Localized velocity structures

Given the non-Gaussian nature of the velocity distribution, we looked for spatially localized variations in the LOS velocity and velocity dispersion distributions. First of all we applied the three 3D tests commonly used to quantify the amount of substructures in galaxy clusters: the  $\Delta$  test (Dressler & Shectman 1988), the  $\alpha$  test (West & Bothun 1990) and the  $\epsilon$  test (Bird 1994).

**Table 3.** The most significant weighted gaps detected in the velocity distribution of the whole cluster sample.

Velocity km s <sup>-1</sup>	Gap	Significance
5742	2.53	1.40%
5835	2.66	1.40%
6619	2.90	0.60%
6880	2.64	1.40%
7059	3.01	0.20%
7542	2.33	3.00%

The  $\Delta$  test is based on the comparison of the local mean velocity,  $V_{local}$ , and the velocity dispersion,  $\sigma_{local}$ , associated to each cluster member (computed using its 10 nearest neighbors) with the mean velocity  $V$ , and dispersion  $\sigma$ , of the whole galaxy sample. For each galaxy, the deviation is defined by:

$$\delta^2 = \frac{11}{\sigma^2} [(V_{local} - V)^2 + (\sigma_{local} - \sigma)^2]$$

The observed cumulative deviation  $\Delta$ , defined as the sum of the  $\delta$ 's for the cluster members, is used to quantify the presence of substructures. As shown by Pinkney et al. (1996) for samples with no substructures, the value of  $\Delta$  is approximately equal to the total number of galaxies, while it is larger in the presence of substructures.

The  $\alpha$  test measures how much the centroid of the galaxy distribution shifts as a result of correlations between the local kinematics and the projected galaxy distribution. The centroid of the whole galaxy distribution is defined as:

$$x_c = \frac{1}{N} \sum_{i=1}^N x_i \quad y_c = \frac{1}{N} \sum_{i=1}^N y_i$$

For each galaxy  $i$  and its 10 nearest neighbors in the velocity space, the spatial centroid is defined as:

$$x_c^i = \frac{\sum_{j=1}^{11} x_j / \sigma_j}{\sum_{j=1}^{11} 1 / \sigma_j} \quad y_c^i = \frac{\sum_{j=1}^{11} y_j / \sigma_j}{\sum_{j=1}^{11} 1 / \sigma_j}$$

where  $\sigma_j$  is the velocity dispersion for galaxy  $j$  and its 10 nearest neighbors in projection. Finally the presence of

**Table 4.** 3D substructure indicators for our sample

Indicator	Value	Prob. of substructures
$\Delta$	206.5	99.8 %
$\alpha$	0.161 Mpc	55.7 %
$\epsilon$	$5.44 \cdot 10^{13} M_\odot$	68.4 %

substructures in the cluster sample is quantified using the  $\alpha$  statistic defined as:

$$\alpha = \frac{1}{N} \sum_{i=1}^N [(x_c^i - x_c)^2 + (y_c^i - y_c)^2]^{1/2}$$

which represents the mean centroid shift for the galaxy cluster. The higher the value of  $\alpha$ , the higher the probability of substructures.

The  $\epsilon$  test quantifies the correlations between the position and the projected mass estimator (Heisler et al. 1985), defined as:

$$M_{PME} = \left( \frac{32}{\pi G N} \right) \sum_{j=1}^N v_{zj}^2 r_j$$

where  $v_{zj}$  is the radial peculiar velocity with respect to the nearest neighbors group (composed by a galaxy and its 10 nearest neighbors) and  $r_j$  is the projected distance from the center of the nearest neighbor group. The substructure statistic is then defined as:

$$\epsilon = \frac{1}{N_{gal}} \sum_{i=1}^N M_{PME}$$

which represents the average mass of the nearest neighbors groups in the cluster. Since galaxies in the nearest neighbors groups have small projected separations,  $\epsilon$  is generally smaller than the global mass estimate.  $\epsilon$  is lower for a cluster with substructures than for a relaxed system. The value and the significance of the above tests are listed in Table 4. These statistical tests are calibrated using 1000 Monte Carlo simulations that randomly shuffle the velocity of galaxies, keeping fixed their observed position, thereby destroying any existing correlation between velocity and position. The probability of subclustering is then given as the fraction of simulated clusters for which the test value is lower (larger for the  $\epsilon$  test) than the observed one. Assuming that these tests reject the null hypothesis if the confidence level is greater than 90%, only the  $\Delta$  test finds evidence of substructures (see Table 4). The local deviations from the global kinematics as measured by the  $\Delta$  test are shown in Fig 3. The positions of galaxies are marked with open circles whose radius scales with their local deviation  $\delta$  from the global kinematics. The presence of a substructure with a high deviation from the global cluster kinematic is evident projected near the cluster core. More insights on the cluster dynamical state can be achieved by comparing the results of the one and three

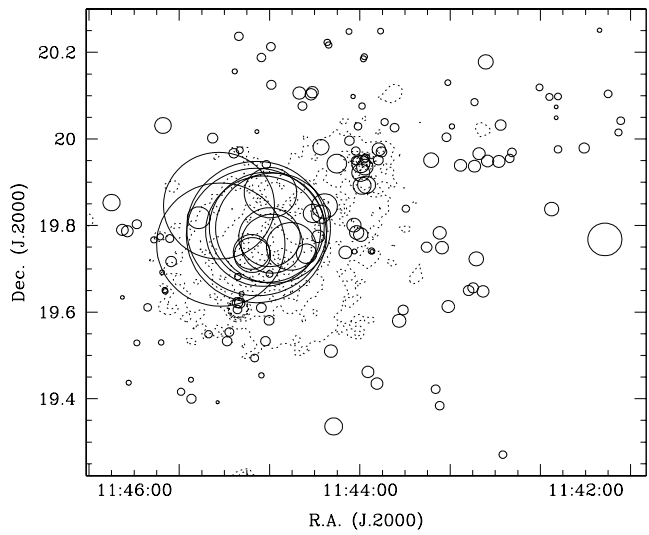


**Fig. 3.** Local deviations from the global kinematics for galaxies in Abell 1367 as measured by the Dressler & Shectman (1988) test. Galaxies are marked with open circles whose radius scales with their local deviation  $\delta$  from the global kinematics. The ROSAT X-ray contours are shown with dotted lines.

dimensional statistical tests with the N-body simulations performed by Pinkney et al. (1996). These authors analyzed how the significance level of statistical tests of substructure varies in different cluster merging scenarios. The deviation of the velocity distribution from a Gaussian and the detection of substructure provided by the  $\Delta$  test suggest that Abell 1367 is in the early merging stage,  $\sim 0.2$  Gyr before core crossing.

## 5. The cluster dynamics

The analysis of the galaxy distribution, of the local mean LOS velocity and of the velocity dispersion give further insight onto the cluster structure. The iso-density map of the cluster members (computed using the 10 nearest neighbors to each point) is shown in Fig.4 (left). The galaxy distribution appears elongated from north-west to south-east with two major density peaks. The highest density region corresponds approximately to the center of the NW X-ray substructure detected by ROSAT (Donnelly et al. 1998), while the secondary density peak is slightly offset from the X-ray cluster center ( $\alpha(J.2000) = 11h44.8m$   $\delta(J.2000) = 19d42m$ , Donnelly et al. 1998). Moreover the south galaxy density peak roughly coincides with the substructure detected by the  $\Delta$  test (see Fig.3) and with the infalling group of star-forming galaxies studied by Gavazzi et al. (2003b).

The iso-density contours superposed on the ROSAT X-ray contours are shown in Fig.4 (right). The region between the two major density peaks coincides with the strong gradient in the gas temperature (see the straight line in Fig.4, right) observed for the first time by ASCA

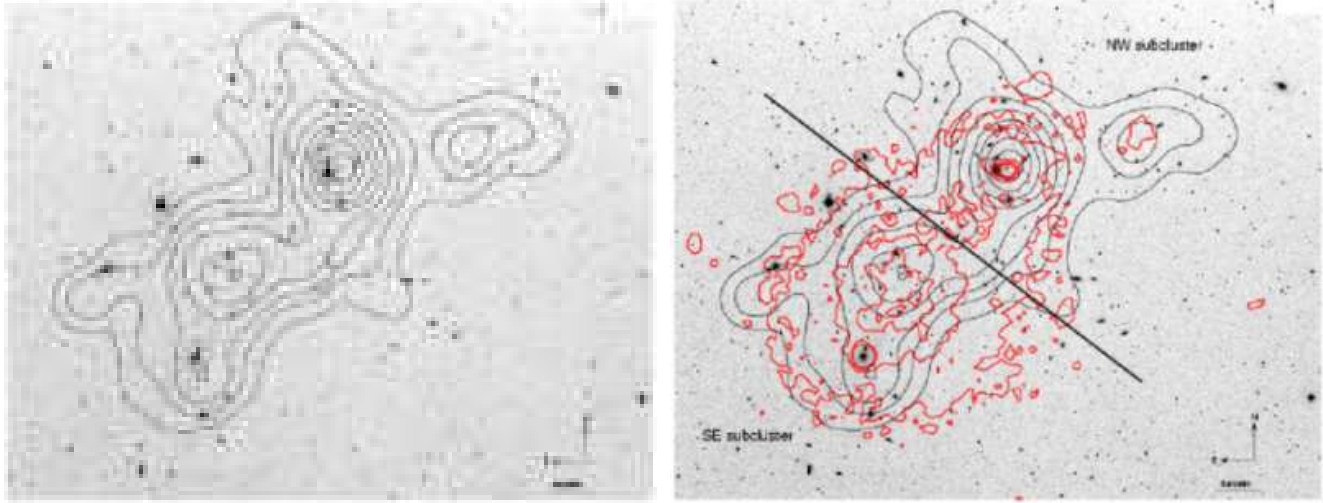


**Fig. 4.** Palomar DSS image of the central region ( $\sim 1.3$  square degrees) of Abell 1367 studied in this work. The iso-density contours for the 146 confirmed cluster members are superposed. The lowest iso-density contour correspond to  $3\sigma$  above the mean density in the field (left). The ROSAT X-ray contours are superposed in red (right). The straight line indicates the position of the abrupt gas temperature gradient detected by ASCA (Donnelly et al. 1998), used to divide our sample into two subclusters: the North-West and the South-East.

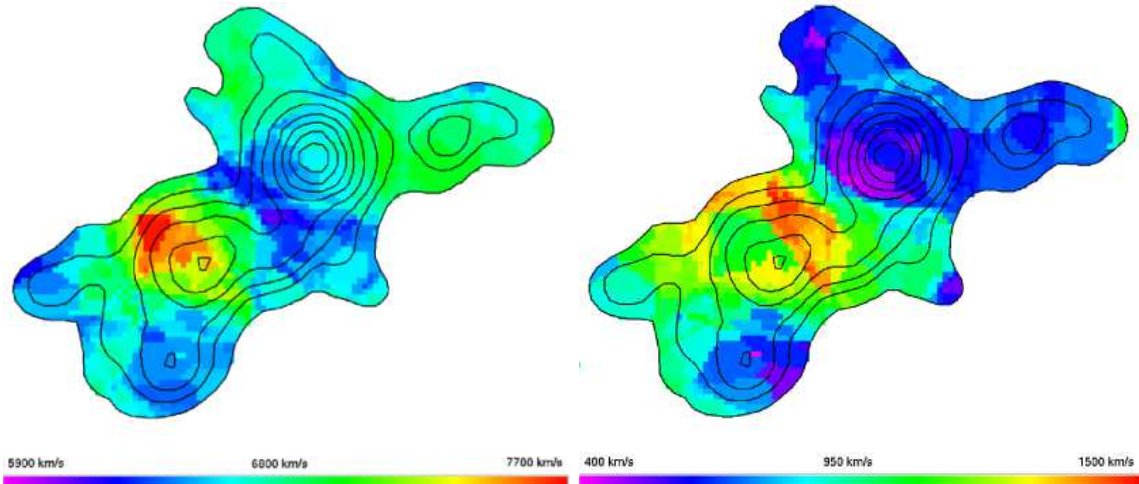


**Fig. 5.** The LOS velocity field (left) and the velocity dispersion field (right) for the whole region studied in this work. The LOS velocity and the velocity dispersion are computed using the 10 nearest neighbors to each pixel, whose size is  $36 \text{ arcsec}^2$ . The iso-density contours for the 146 confirmed cluster members are superposed in black.

(Donnelly et al. 1998) and recently confirmed by Chandra (Sun & Murray 2002). This abrupt temperature change is strongly suggestive of a shock which has generated during a collision between two substructures, probably associated with the SE and the NW galaxy density peaks. In fact N-body simulations show that temperature structures and X-ray morphology similar to the one observed in Abell 1367 are typical of clusters at an early merging phase ( $\sim 0.25$  Gyr before core crossing) (Schindler & Mueller 1993; Gomez et al. 2002).

The merging scenario is further supported by the LOS velocity and velocity dispersion fields (computed using the 10 nearest neighbors to each point) shown in Fig. 5. The SE subcluster has higher LOS velocity and velocity dis-

persion than the NW substructure. The region with the highest LOS velocity and velocity dispersion lies  $\sim 6$  arcmin N from the X-ray cluster center and it coincides with the substructure detected by the  $\Delta$  test. This result points out the presence of a group of galaxies infalling in the SE cluster core (see Sec. 5.2).

Thus the NW subcluster appears as a relaxed system with the lowest velocity dispersion among the whole sample; on the other hand the SE subcluster appears far from relaxation, and it is probably experiencing a multiple merging event.

We use the position of the gas temperature gradient, shown by the straight line in Fig.4 (right), to divide our sample into two regions and to study separately the dy-

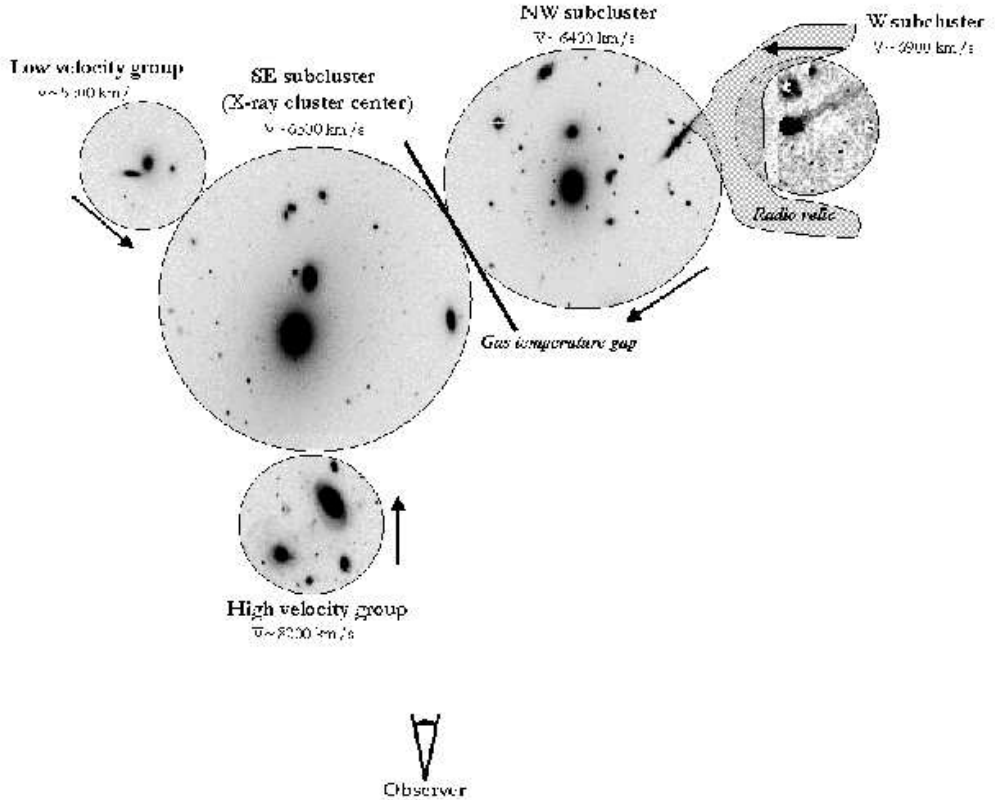


**Fig. 6.** A 3D sketch of Abell 1367 summarizing the various sub-components described in Section 5. The cluster is viewed from its near side, as suggested by the eyeball indicating the observer's position.

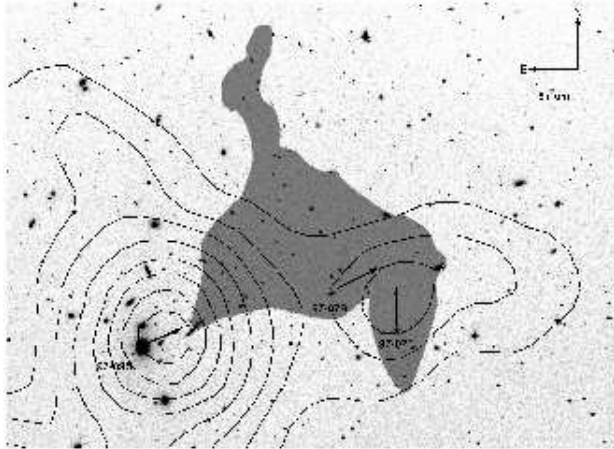


**Fig. 7.** Blow-up of the NW substructure of Abell 1367. The arrows indicate the direction of radio head tails associated with 97-079 and 97-073 and the orientation of the NAT radio galaxy 97-095. The dashed region shows the distribution of the diffuse cluster radio relic (Gavazzi 1978). The iso-density contours for the 146 confirmed cluster members are superposed.

namical properties of the two subclusters.

A sketch of the cluster dynamical model discussed in the next section is given in Fig.6.

### 5.1. The North-West subcluster

The NW subcluster is composed of 86 galaxies and includes two density peaks: the highest and a secondary one located at the western periphery of the subcluster (labeled as W subcluster in Fig.6), with a weak X-ray counterpart. It has a similar mean location ( $C_{BI} = 6480 \pm 87 \text{ km s}^{-1}$ ) and a lower scale ( $S_{BI} = 770 \pm 60 \text{ km s}^{-1}$ ) than the whole cluster.

Fig.8 shows the LOS velocity distribution of this subcluster. The W test rejects the Gaussian hypothesis at a confidence level of 39%. Thus the LOS velocity distribution is consistent with a Gaussian distribution, suggesting that this subcluster is a virialized system. Moreover its increasing velocity dispersion profile (see Fig. 9) is consistent with a relaxed cluster undergoing two body relaxation in the dense central region, with circular velocities in the center and more isotropic velocities in the external regions (Girardi et al. 1998).

However this subcluster also shows some evidences of merging (see Fig.7). The brightest galaxy of this cloud CGCG97-095 (NGC3842), located  $\sim 2$  arcmin SE from the NW density peak, is a radio galaxy classified as a narrow-angle tail (NAT) (Bliton et al. 1998). The tail orientation (indicated with an arrow in Fig. 7) suggests that this galaxy (and the associated substructure) is moving from north-west to south-east, toward the main cluster core.

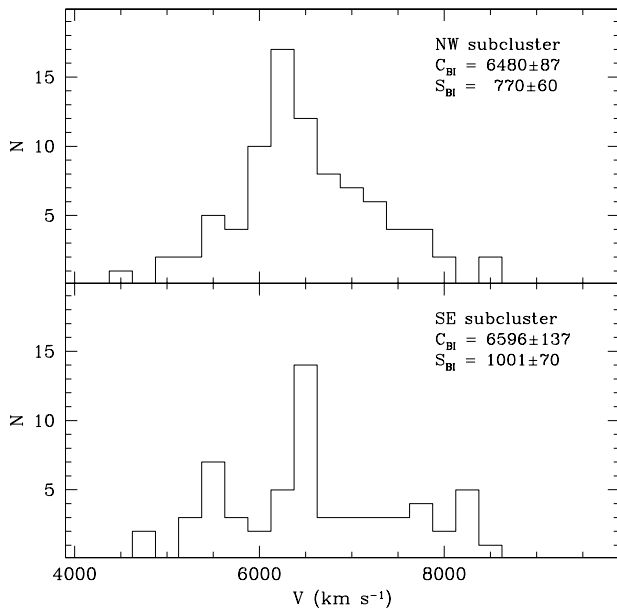


**Fig. 8.** The LOS velocity distribution for galaxies in the NW (upper) and in the SE (lower) subclusters.

Moreover two CGCG (Zwicky et al. 1961-1968) galaxies, 97-073 and 97-079, show features consistent with the infall scenario. Gavazzi et al. (1995, 2001) found that both galaxies have their present star formation enhanced along peripheral HII regions which developed at the side facing the direction of motion through the cluster IGM. Their neutral hydrogen is significantly displaced in the opposite side (Dickey & Gavazzi 1991), where 50 kpc long tails are detected both in the light of the synchrotron radiation (Gavazzi & Jaffe 1987) and in H $\alpha$  (Gavazzi et al. 2001). The observational scenario is consistent with the idea that ram-pressure (Gunn & Gott 1972) is enhancing for a limited amount of time the star formation of galaxies that are entering the cluster medium for the first time.

However these two galaxies appear not directly associated with the center of the NW subcluster since they lie at a projected distance of  $\sim 0.34$  Mpc from the main density peak (see Fig.7). Moreover their large distance ( $\sim 0.48$  Mpc) from the shock front observed in X-ray between the NW and the SE substructure indicates that these objects do not belong to the main galaxy density peak infalling into the cluster center. Conversely they are at a projected distance of only 0.08 Mpc from the center of the W subcluster, suggesting that they are associated with this sub-cloud.

For these reasons we consider an alternative scenario in which these two galaxies belong to a secondary substructure infalling into the NW substructure from the western side (see Fig. 6). This picture is supported by the presence of the extended radio relic detected both in X-ray and radio continuum in this region (Gavazzi 1978; Gavazzi & Trinchieri 1983). Cluster radio halos contain fossil radio plasma, the former outflow of a radio galaxy,

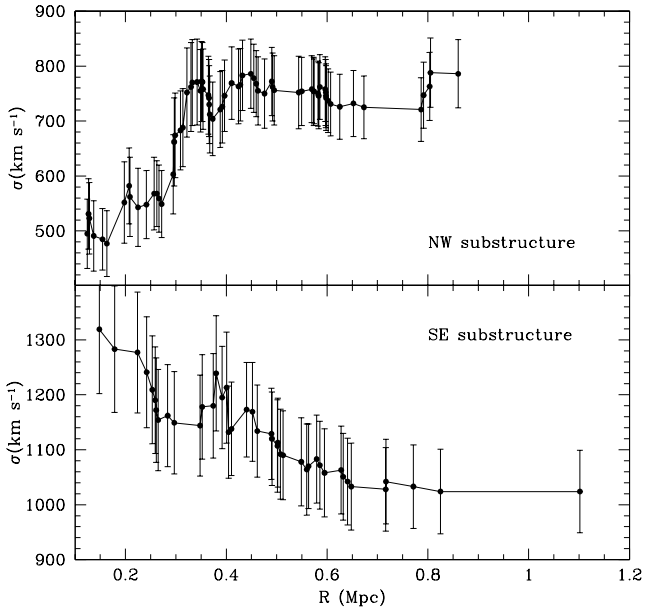


**Fig. 9.** The velocity dispersion radial profile of the NW (upper) and the SE (lower) subclusters.

that has been revived by shock compression during cluster merging (Enßlin et al. 1998; Enßlin & Brüggen 2002). The radio relic observed in Abell 1367 extends, south-west to north-east, from 97-073 to 127-040 with a projected extent of 0.8 Mpc (see Fig.7). The age of its electrons is estimated to be  $\sim 0.2$  Gyr (Enßlin et al. 1998). The only plausible source of high energy electrons available in this region is the NAT galaxy 97-095, presently at  $\sim 0.25$  Mpc from the relic and whose tails point exactly in the relic direction. Assuming that the fossil radio halo originated from 97-095, we find that the infall velocity of this galaxy into the SE subcluster is  $V \sim 1250$  km s $^{-1}$ , consistent with the typical infall velocity of cluster galaxies. Thus the presence of the radio relic results consistent with a merging scenario in which the W subcluster, containing 97-079 and 97-073, is infalling into the NW substructure, compressing the plasma ejected from 97-095 and re-accelerating the electrons to relativistic energies.

## 5.2. The South-East subcluster

The SE cloud is composed of 60 galaxies associated with the X-ray cluster center. It has the highest LOS velocity and dispersion of the whole sample (see Fig.5) with a location  $C_{BI} = 6596 \pm 137$  km s $^{-1}$  and a scale  $S_{BI} = 1001 \pm 70$  km s $^{-1}$ . Its velocity distribution, shown in Fig. 8, appears significantly non-Gaussian. The W test rejects the Gaussian hypothesis at a confidence level of 96.8%, supporting the idea that the cluster center is far from relaxation. This is in agreement with the decreasing velocity dispersion profile of this region (see Fig.9), consistent with isotropic velocities in the center and radial velocities in the external regions, as expected in the case of galaxy infall

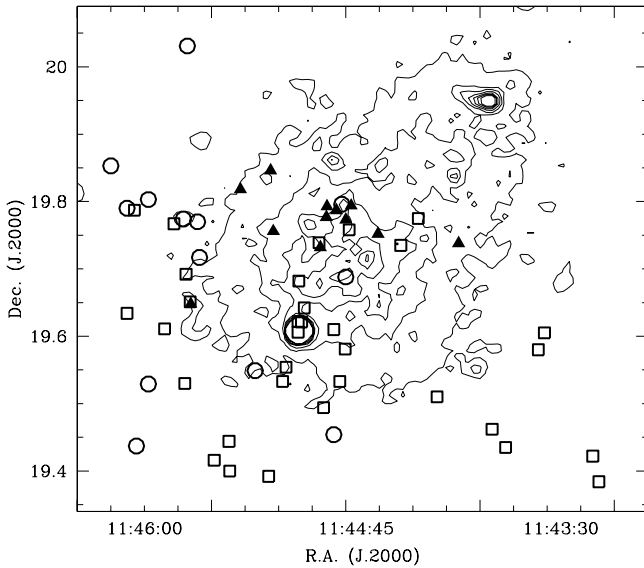


**Fig. 10.** The distribution of galaxies belonging to the South-East subcluster. Triangles indicate galaxies with LOS velocity  $> 7500 \text{ km s}^{-1}$ , circles galaxies with LOS velocity  $< 5800 \text{ km s}^{-1}$  and squares galaxies with LOS velocity comprises in the range  $5800 \text{ km s}^{-1} < V < 7500 \text{ km s}^{-1}$ . The ROSAT X-ray contours are shown.

onto the cluster (Girardi et al. 1998).

The velocity distribution of Fig. 8 has three peaks at  $\sim 5500 \text{ km s}^{-1}$ ,  $\sim 6500 \text{ km s}^{-1}$  and  $\sim 8200 \text{ km s}^{-1}$  respectively, probably associated with three separate groups. Moreover we remark that the galaxy gaps between the three peaks are fairly consistent with two of the most significant weighted gaps detected in the global velocity distribution ( $V \sim 5800 \text{ km s}^{-1}$  and  $V \sim 7500 \text{ km s}^{-1}$ ).

In order to check for any position-velocity segregation, we divide the SE subcluster in three groups according to their LOS velocity: galaxies with  $V < 5800 \text{ km s}^{-1}$  belong to the low velocity group, galaxies with  $V > 7500 \text{ km s}^{-1}$  belong to the high velocity group and galaxies with intermediate velocity belong to the SE subcluster.

The projected distribution of the three groups is shown in Fig.10. The high-velocity group ( $V \sim 8200 \text{ km s}^{-1}$ , triangles) appears segregated in the northern part of the SE cloud, extending  $\sim 20$  arcmin in right ascension but only  $\sim 7$  arcmin in declination. It is associated with the substructure detected by the  $\Delta$  test (see Fig. 3) and with the infalling group of star-forming galaxies recently discovered by Sakai et al. (2002) and by Gavazzi et al. (2003b). Its spatial segregation and high star formation activity suggest that this group is a separate unit infalling into the cluster, probably from the near side (see Fig. 6). It is remarkable that Sun & Murray (2002), using Chandra observations of the cluster center, discovered a ridge-like structure around the cluster center,  $\sim 6$  arcmin south from the center of the high velocity group, probably associated with a compact merging subcluster (perhaps this group)

penetrating the SE cluster core.

The low-velocity group ( $V \sim 5500 \text{ km s}^{-1}$ , circles in Fig.10) seems segregated in the eastern part of the cloud, perhaps infalling from the eastern side into the cluster core (Fig. 6). This scenario is also supported by the detection of cool gas streaming into the cluster core from the eastern side (Forman et al. 2003), probably associated with this low velocity group of galaxies.

Galaxies with  $V \sim 6500 \text{ km s}^{-1}$  (squares in Fig.10) are homogeneously distributed over the SE subcluster, representing its virialized galaxy population. However the brightest galaxy in this group 97-127 (NGC3862) is a NAT radio galaxy with very extended radio tails pointing in the direction of the low velocity group (Gavazzi et al. 1981), suggesting motion relative to the IGM.

The velocity-space segregation observed in the SE subcluster suggests that the cluster center is experiencing multiple merging of at least two separate groups, supporting the idea that it is far from relaxation. This picture is consistent with the high gas entropy in this region, since in absence of a cool dense core the substructures infalling into the major cluster can penetrate deep inside, disturbing the cluster core dynamics (Churazov et al. 2003).

A sketch of the various substructures identified in Abell 1367 by the present study, is given in Fig. 6. Five substructures are detected. Two clouds, the NW and SE subclusters, are in the early merging phase, meanwhile three smaller groups are infalling into Abell 1367. The W sub-cloud, associated with the head-tail systems 97-073/79, is probably infalling into the NW subcluster, exciting the radio relic observed in between the two structures. The other two groups are infalling into the SE subcluster: the low velocity group from the eastern side, while the high velocity group from the near side.

## 6. Star formation activity in the infalling groups

The dynamical study presented in the previous sections indicates that Abell 1367 is a dynamically young cluster in the early stage of a multiple merging event involving at least five substructures. Since merging is expected to trigger star formation in cluster galaxies (Bekki 1999), we study separately the spatial and velocity distribution of the star forming galaxies. Only 49 out of the 146 cluster members show recent star formation activity (e.g. H $\alpha$  line in emission, Iglesias-Páramo et al. 2002; Gavazzi et al. 2003a; Cortese et al., in preparation). Fig.11 shows the LOS velocity distribution of galaxies divided into emission line (upper panel) and non emission line (lower panel) galaxies. The star forming sample has higher location and scale ( $C_{BI} = 6704 \pm 168 \text{ km s}^{-1}$ ,  $S_{BI} = 1076 \pm 76 \text{ km s}^{-1}$ ) than the quiescent sample ( $C_{BI} = 6446 \pm 79 \text{ km s}^{-1}$ ,  $S_{BI} = 738 \pm 58 \text{ km s}^{-1}$ ). According to a two-sample Kolmogorov-Smirnov test the two velocity distributions have only  $\sim 5\%$  probability of being consistent, suggesting a different origin and/or evolution. We remark that, if the star forming galaxies are infalling onto the cluster along radial orbits, their velocity

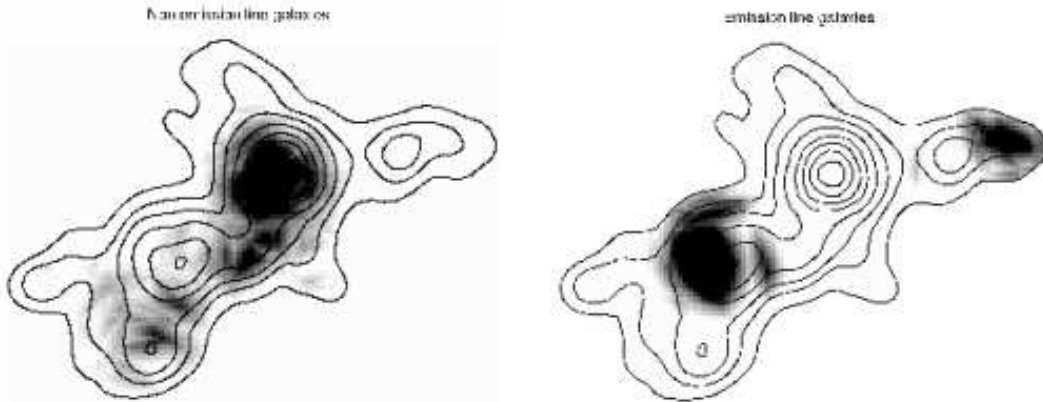


**Fig. 12.** Projected density map of non emission line (left) and emission line (right) galaxies in Abell 1367. The iso-density contours of the 146 confirmed cluster members are superposed.

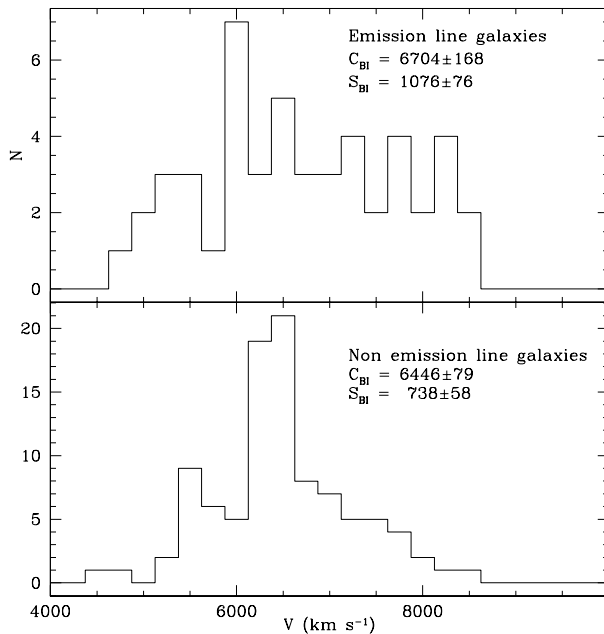


**Fig. 11.** The LOS velocity distribution for emission line (upper) and non emission line galaxies (lower) in the whole cluster sample.

dispersion should be  $\sim \sqrt{2}$  times the velocity dispersion of the relaxed sample, as observed in this case. This result suggests that star forming systems are an infalling population while the non-star forming galaxies represent the virialized cluster population.

The projected density distribution of star forming and non star forming is shown in Fig.12. The highest density of non emission line systems is observed near the center of the NW substructure. This morphological segregation further supports the idea that the NW cloud is a relaxed system merging for the first time into the SE subcluster.

The emission line galaxies have a different distribution. The highest density of star forming systems is in the infalling groups, i.e. in the high velocity group infalling into the SE subcluster and in the W cloud infalling into the

**Table 5.** Mass estimate for Abell 1367

Sample	$R_H$ Mpc	$M_V$ $10^{14} M_\odot$	$M_{PM}$ $10^{14} M_\odot$
A1367 all types	0.41	$7.04 \pm 0.90$	$7.82 \pm 2.50$
A1367 non-star forming	0.37	$4.35 \pm 0.70$	$5.11 \pm 0.90$
A1367 NW all types	0.30	$3.87 \pm 0.62$	$6.12 \pm 1.52$
A1367 NW non-star forming	0.24	$2.47 \pm 0.46$	$3.29 \pm 0.59$
A1367 SE all types	0.27	$5.80 \pm 0.88$	$6.87 \pm 1.20$
A1367 SE non-star forming	0.26	$3.90 \pm 0.83$	$5.58 \pm 0.74$

NW substructure, suggesting that their interaction with the cluster environment is triggering some star formation activity. Indeed in these systems the fraction of star forming galaxies lies between 64% and 36%, decreasing to 31% in the NW substructure and to 20% in the SE subcluster.

## 7. Cluster mass

The virial theorem is the standard tool used to estimate the dynamical mass of galaxy clusters. Under the assumptions of spherical symmetry and hydrostatic equilibrium and if the mass distribution follows the distribution of the observed galaxies independent of their luminosity, the total gravitational mass of a cluster is given by

$$M_V = \frac{3\pi}{G} \sigma^2 R_H$$

where  $\sigma$  is the galaxy velocity dispersion and  $R_H$  is the cluster mean harmonic radius:

$$R_H = \frac{N(N-1)}{\sum_{i>j} R_{ij}^{-1}}$$

where  $N$  is the total number of galaxies.

An alternative approach is to use the projected mass estimator (Heisler et al. 1985), defined as

$$M_{PM} = \frac{32}{\pi G N} \sum_i V_i^2 R_i$$

where  $V_i$  is the observed radial component of the velocity of the  $i$  galaxy with respect to the systemic cluster velocity, and  $R_i$  is its projected separation from the cluster center. The numerical factor 32 assumes that galaxy orbits are isotropic. In case of purely radial or purely circular orbits this factor becomes 64 or 16 respectively. Mass estimates obtained using the two above methods and their uncertainties are listed in Table 5. We remark that these mass estimates are probably biased by the dynamical state of Abell 1367, which appears far from virialization. In particular the presence of substructures leads to an overestimate of the cluster mean harmonic radius and velocity dispersion, and thus of the virial mass (Pinkney et al. 1996). For this reason the mass derived for the whole cluster and for the SE and NW subclusters separately is probably overestimated. Assuming that the early type sample represents the virialized cluster population (see previous section), we also derive mass estimates for the three dynamical units using the non star forming systems only.

For all the studied samples the viral mass estimates are affected by smaller uncertainties and yield smaller values than the projected mass estimates. This can be due to the contamination by interlopers (Heisler et al. 1985) or, more probably, to the assumption of isotropic orbits. Indeed assuming purely radial or circular orbits the mass estimate varies by a factor of 2, becoming consistent with the viral mass.

The mass inferred from the non-star forming population are, as expected, systematically lower than the ones obtained from all types. The value obtained for the whole sample is consistent with the mass estimates available in the literature ( $M_V = 7.26 \pm 1.40 \ 10^{14} M_\odot$  Girardi et al. 1998;  $M_V = 6.07 \pm 0.93 \ 10^{14} M_\odot$ ,  $M_{PM} = 6.28 \pm 0.80 \ 10^{14} M_\odot$  Rines et al. 2003).

## 8. Two-Body Analysis

In this section we investigate whether the two clouds A1367NW, A1367SE and the three groups infalling into the SE and NW subclusters form gravitationally bound systems. For each system we apply the two-body analysis described by Beers et al. (1991). The two subclumps are treated as point masses moving on radial orbits. They are assumed to start their evolution at time  $t=0$  with zero separation, and are moving apart or coming together for the first time in their history. For bound radial orbits, the parametric solutions to the equations of motion are:

$$R = \frac{R_m}{2}(1 - \cos \chi)$$

$$t = \left( \frac{R_m^3}{8GM} \right)^{1/2} (\chi - \sin \chi)$$

$$V = \left( \frac{2GM}{R_m} \right)^{1/2} \frac{\sin \chi}{(1 - \cos \chi)}$$

where  $R$  is the components separation at time  $t$ , and  $V$  is their relative velocity.  $R_m$  is the separation of the subclusters at maximum expansion and  $M$  is the total mass

of the system. Similarly, the parametric solutions for the unbound case are:

$$R = \frac{GM}{V_\infty^2} (\cosh \chi - 1)$$

$$t = \frac{GM}{V_\infty^3} (\sinh \chi - \chi)$$

$$V = V_\infty \frac{\sinh \chi}{(\cosh \chi - 1)}$$

where  $V_\infty$  is the asymptotic expansion velocity.

The system parameters  $V$  and  $R$  are related to the observables  $V_{rel}$  (the LOS relative velocity) and  $R_p$  (the projected separation) by:

$$V_{rel} = V \sin \alpha, \quad R_p = R \cos \alpha$$

where  $\alpha$  is the angle between the plane of the sky and the line joining the centers of the two components. The two systems are thus closed by setting the present time to  $t_0 = 13$  Gyr (the age of the Universe in a  $\Omega_m=0.3$  and  $\Omega_\lambda=0.7$  cosmology) and solved iteratively to determine the projection angle as a function of  $V_{rel}$ .

We determine two solutions for each two-body model, assuming two extreme values for the total mass of each system ranging from the viral mass of the non-star forming population to the viral mass of the whole cluster. Table 6 summarizes the adopted parameters of the two-body analysis, and Fig. 13 shows the computed solutions in the  $(\alpha, V_{rel})$  plane. The vertical lines represent the observed values of  $V_{rel}$  and the dashed regions their associated  $1\sigma$  uncertainties.

The solutions have three different regimes: an unbound-outgoing regime (UO), a bound-outgoing regime (BO) and a bound-ingoing regime (BI). It is easy to show that the unbound solutions will lie in the region of the  $(\alpha, V_{rel})$  plane where:

$$V_{rel}^2 R_p \leq 2GM_{tot} \sin^2 \alpha \cos \alpha.$$

The dotted lines in Fig. 13 show the dividing line between bound and unbound regions.

In the BO regime, the two subclumps are still separating and have not yet reached the maximum expansion.

The BI regime describes the system after maximum expansion. For each  $V_{rel}$ , there are two corresponding values of  $\alpha$ , a large and a small one. The large value assumes that the substructures are far apart, with low relative velocity, while the small value implies that the subclusters are close together near the plane of the sky (see Fig. 7 in Beers et al. 1991). Thus we split the BI regime into two branches, called  $BI_a$  and  $BI_b$ .

The probability of each solution, computed following the procedure described by Beers et al. (1991), is given in Table 6. Our result is that the *A1367NW/SE* and the *A1367SE/High Velocity group* systems are bound with 100% probability and presently infalling with 96% and 100% probability respectively. The *A1367NW/W* and the *A1367SE/Low Velocity group* systems are bound at 99%

**Table 6.** Two-body model parameters

System	$M_{\text{tot}}$ $10^{14} M_{\odot}$	$V_{\text{rel}} \pm \Delta V_{\text{rel}}$ km s $^{-1}$	$R_p$ Mpc	Solution Probability			
				BI <sub>a</sub> %	BI <sub>b</sub> %	BO %	UO %
A1367NW/SE	7.04	$84 \pm 162$	0.45	57	40	3	0
	4.35	$84 \pm 162$	0.45	55	41	4	0
A1367NW/W	7.04	$500 \pm 200$	0.37	57	40	2	1
	2.47	$500 \pm 200$	0.37	56	41	2	1
A1367SE/Low Vel. gr.	7.04	$1000 \pm 200$	0.38	58	40	0	2
	3.90	$1000 \pm 200$	0.38	57	39	0	4
A1367SE/High Vel. gr.	7.04	$1500 \pm 200$	0.08	56	44	0	0
	3.90	$1500 \pm 200$	0.08	58	42	0	0

and 96% probability respectively. We conclude that all systems constituting Abell 1367 are gravitationally bound at  $\geq 96\%$  probability.

## 9. Conclusions

We present a dynamical analysis of the central  $\sim 1.3$  square degrees of the galaxy cluster Abell 1367, based on 273 redshift of which 119 are new measurements. The LOS velocity distribution of the 146 cluster members is significantly non Gaussian, suggesting that the cluster is dynamically young. The member galaxies show an elongated distribution along the NW-SE direction with two major density peaks, consistent with the X-ray morphology. The strong difference in the LOS velocity and velocity dispersion of the two density peaks, the abrupt gas temperature gradient detected in X-rays and the 3D statistical tests support a merging scenario involving at least two subclusters. Moreover the dynamical properties of the NW and SE clouds suggest an even more complex picture, summarized in Fig. 6. At least another group of star forming galaxies (the high velocity group) infalling into the cluster core is detected, suggesting a multiple merging event. Furthermore our analysis suggests the presence of two other groups infalling into the cluster center. In the North-West part of Abell 1367 a group of galaxies (W subcluster), associated with the infalling galaxies 97-073/79 and with the radio relic observed in this region, is probably merging with the relaxed core of the NW subcluster. In the South part another group (the low velocity group) is infalling from the eastern side into the disturbed core of the SE subcluster. These three subgroups have a higher fraction of star forming galaxies than the cluster core, as expected during the early phase of merging events.

The multiple merging scenario is consistent with the location of Abell 1367 being at the intersection of two filaments, the first extending roughly 100 Mpc from Abell 1367 toward Virgo (West & Blakeslee 2000) and the second extending between Abell 1367 and Coma (as a part of the Great Wall, Zabludoff et al. 1993). As predicted by Katz & White (1993) this is the natural place for Abell 1367 to evolve into a rich relaxed cluster.

*Acknowledgements.* We thank the referee, R. Hank Donnelly, for his useful comments which helped us to improve and strengthen the paper. We thank Paolo Franzetti for his help during the preparation of the AF2-WYFFOS configurations and Timothy Beers for kindly providing the program ROSTAT. The TACS of the William Herschel, Loiano and Cananea telescopes are acknowledged for the generous time allocation to this project. This work could not be completed without the NASA/IPAC Extragalactic Database (NED) which is operated by the Jet Propulsion Laboratory, Caltech under contract with NASA. This research has made use of the GOLD Mine Database, operated by the Universitá degli Studi di Milano-Bicocca.

## References

- Bechtold, J., Forman, W., Jones, C., et al. 1983, ApJ, 265, 26
- Beers, T. C., Flynn, K., & Gebhardt, K. 1990, AJ, 100, 32
- Beers, T. C., Gebhardt, K., Forman, W., Huchra, J. P., & Jones, C. 1991, AJ, 102, 1581
- Bekki, K. 1999, ApJ, 510, L15
- Bird, C. M. 1994, AJ, 107, 1637
- Bird, C. M. & Beers, T. C. 1993, AJ, 105, 1596
- Bliton, M., Rizza, E., Burns, J. O., Owen, F. N., & Ledlow, M. J. 1998, MNRAS, 301, 609
- Churazov, E., Forman, W., Jones, C., & Böhringer, H. 2003, ApJ, 590, 225
- Cortese, L., Gavazzi, G., Iglesias-Paramo, J., Boselli, A., & Carrasco, L. 2003, A&A, 401, 471
- Dickey, J. M. & Gavazzi, G. 1991, ApJ, 373, 347
- Donnelly, R. H., Markevitch, M., Forman, W., et al. 1998, ApJ, 500, 138
- Dressler, A. & Shectman, S. A. 1988, AJ, 95, 985
- Enßlin, T. A., Biermann, P. L., Klein, U., & Kohle, S. 1998, A&A, 332, 395
- Enßlin, T. A. & Brüggen, M. 2002, MNRAS, 331, 1011
- Forman, W., Churazov, E., David, L., et al. 2003, astro-ph/0301476
- Gavazzi, G. 1978, A&A, 69, 355
- Gavazzi, G., Boselli, A., Donati, A., Franzetti, P., & Scudegger, M. 2003a, A&A, 400, 451

Gavazzi, G., Boselli, A., Mayer, L., et al. 2001, ApJ, 563, L23

Gavazzi, G., Carrasco, L., & Galli, R. 1999, A&AS, 136, 227

Gavazzi, G., Contursi, A., Carrasco, L., et al. 1995, A&A, 304, 325

Gavazzi, G., Cortese, L., Boselli, A., et al. 2003b, ApJ, 597, 210

Gavazzi, G. & Jaffe, W. 1987, A&A, 186, L1

Gavazzi, G., Perola, G. C., & Jaffe, W. 1981, A&A, 103, 35

Gavazzi, G. & Trinchieri, G. 1983, ApJ, 270, 410

Girardi, M., Giuricin, G., Mardirossian, F., Mezzetti, M., & Boschin, W. 1998, ApJ, 505, 74

Gomez, P. L., Loken, C., Roettiger, K., & Burns, J. O. 2002, ApJ, 569, 122

Grebenev, S. A., Forman, W., Jones, C., & Murray, S. 1995, ApJ, 445, 607

Gunn, J. E. & Gott, J. R. I. 1972, ApJ, 176, 1

Heisler, J., Tremaine, S., & Bahcall, J. N. 1985, ApJ, 298, 8

Iglesias-Páramo, J., Boselli, A., Cortese, L., Vilchez, J. M., & Gavazzi, G. 2002, A&A, 384, 383

Iglesias-Páramo, J., Boselli, A., Gavazzi, G., Cortese, L., & Vilchez, J. M. 2003, A&A, 397, 421

Jones, C., Mandel, E., Schwarz, J., et al. 1979, ApJ, 234, L21

Katz, N. & White, S. D. M. 1993, ApJ, 412, 455

Pinkney, J., Roettiger, K., Burns, J. O., & Bird, C. M. 1996, ApJS, 104, 1

Rines, K., Geller, M. J., Kurtz, M. J., & Diaferio, A. 2003, AJ, 126, 2152

Sakai, S., Kennicutt, R. C., van der Hulst, J. M., & Moss, C. 2002, ApJ, 578, 842

Schindler, S. & Mueller, E. 1993, A&A, 272, 137

Struble, M. F. & Rood, H. J. 1999, ApJS, 125, 35

Sun, M. & Murray, S. S. 2002, ApJ, 576, 708

Tonry, J. & Davis, M. 1979, AJ, 84, 1511

West, M. J. & Blakeslee, J. P. 2000, ApJ, 543, L27

West, M. J. & Bothun, G. D. 1990, ApJ, 350, 36

West, M. J., Villumsen, J. V., & Dekel, A. 1991, ApJ, 369, 287

Yahil, A. & Vidal, N. V. 1977, ApJ, 214, 347

Zabludoff, A. I., Geller, M. J., Huchra, J. P., & Ramella, M. 1993, AJ, 106, 1301

Zwicky, F., Herzog, E., & Wild, P. 1961-1968, in Catalogue of Galaxies and of Clusters of Galaxies", California Institute of Technology

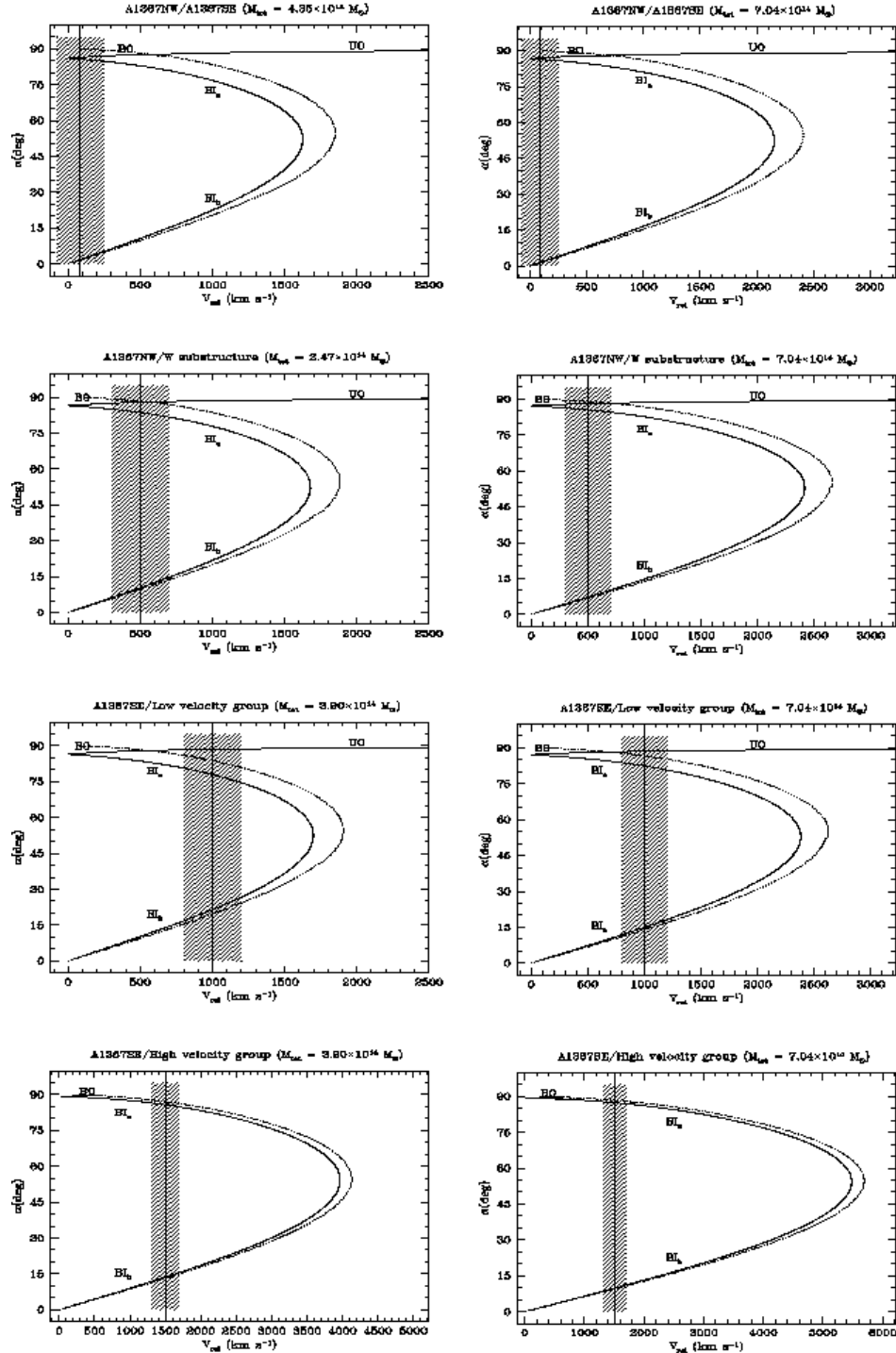


**Fig. 13.** The bound and unbound orbit regions in the  $(V_{rel}, \alpha)$  plane. The bound-incoming solutions ( $BI_a$  and  $BI_b$ ), the bound-outgoing solutions ( $BO$ ) and the unbound-outgoing ( $UO$ ) solutions are indicated with solid lines. The dotted lines show the dividing line between bound and unbound regions. The vertical solid lines represent the observed  $V_{rel}$  and the dashed regions their associated  $1\sigma$  uncertainty.

**Table 7.** The 119 new redshift measurements

Name	R.A. (J.2000)	Dec. (J.2000)	r' mag	V km s <sup>-1</sup>	Tel.	Name	R.A. (J.2000)	Dec. (J.2000)	r' mag	V km s <sup>-1</sup>	Tel.
114000+195426	114000.62	195426.7	15.98	10883	CAN	114356+201404	114356.80	201404.9	18.42	72058	WHT
114159+193227	114159.52	193227.3	15.63	21228	CAN	114357+201122	114357.69	201122.7	17.06	5348	WHT
114200+195846	114200.83	195846.0	17.09	6420	WHT	114358+195330	114358.86	195330.2	19.22	6200	WHT
114208+191905	114208.01	191905.0	19.04	23456	WHT	114359+195630	114359.51	195630.8	20.37	6992	WHT
114212+195650	114212.47	195650.3	17.73	20278	WHT	114402+194742	114402.65	194742.7	17.52	43665	WHT
114213+193001	114213.87	193001.6	16.92	23641	WHT	114403+200552	114403.70	200552.6	15.80	5698	WHT
114215+200427	114215.59	200427.0	19.20	6100	WHT	114404+192922	114404.17	192922.8	18.59	53335	WHT
114219+200548	114219.15	200548.0	16.45	6841	CAN	114404+195956	114404.65	195956.6	17.33	33830	WHT
114224+195329	114224.39	195329.8	18.29	31440	WHT	114407+193850	114407.21	193850.9	17.10	20877	WHT
114224+191157	114224.48	191157.0	16.39	28546	CAN	114407+193143	114407.71	193143.1	18.44	53424	WHT
114226+194317	114226.24	194317.1	17.50	23416	WHT	114412+195503	114412.22	195503.9	17.65	20916	WHT
114230+191447	114230.62	191447.5	18.60	27304	WHT	114412+195633	114412.27	195633.4	17.02	6244	WHT
114230+192553	114230.95	192553.8	17.80	45683	WHT	114412+201119	114412.92	201119.7	19.25	74731	WHT
114238+194718	114238.24	194718.6	17.04	25610	WHT	114415+193037	114415.25	193037.5	16.58	6502	WHT
114239+195145	114239.78	195145.9	19.06	53710	WHT	114415+193012	114415.33	193012.3	18.27	35227	WHT
114240+195627	114240.26	195627.5	18.63	19946	WHT	114417+194543	114417.28	194543.9	18.14	66264	WHT
114243+191615	114243.81	191615.8	18.72	5312	WHT	114422+194628	114422.16	194628.2	15.70	6527	CAN
114249+193935	114249.85	193935.1	19.14	72429	WHT	114426+195951	114426.10	195951.5	16.98	30102	WHT
114250+193955	114250.47	193955.7	19.22	13759	WHT	114430+194258	114430.30	194258.3	18.78	40347	WHT
114252+195656	114252.17	195656.4	16.69	5936	WHT	114432+195341	114432.19	195341.6	18.89	42649	WHT
114254+193851	114254.40	193851.3	17.17	6406	WHT	114432+194734	114432.98	194734.6	18.82	71100	WHT
114254+194033	114254.93	194033.6	18.87	71389	WHT	114447+201248	114447.20	201248.5	18.17	6699	WHT
114258+194321	114258.13	194321.1	18.98	6523	WHT	114449+195628	114449.72	195628.9	16.70	5539	WHT
114258+194053	114258.37	194053.9	19.25	71436	WHT	114501+195504	114501.97	195504.5	18.79	45708	WHT
114258+194644	114258.53	194644.2	19.00	88274	WHT	114503+193831	114503.00	193831.2	16.76	6193	LOI
114258+195612	114258.94	195612.7	18.41	7059	WHT	114503+194743	114503.14	194743.9	17.91	23374	WHT
114259+194801	114259.71	194801.1	18.92	71600	WHT	114504+201412	114504.25	201412.2	18.31	5477	WHT
114300+192515	114300.65	192515.2	18.42	53145	WHT	114505+194057	114504.83	194056.9	15.67	6506	LOI
114301+194758	114301.24	194758.9	18.67	72572	WHT	114506+200849	114506.38	200849.9	19.23	3822	WHT
114301+195313	114301.97	195313.5	18.61	46935	WHT	114509+194845	114509.38	194845.4	17.49	19831	WHT
114307+192807	114307.13	192807.3	17.37	32298	WHT	114509+193316	114509.40	193316.2	15.80	7409	LOI
114307+193029	114307.16	193029.8	17.93	23763	WHT	114509+194526	114509.65	194526.9	16.90	19834	WHT
114310+192526	114310.09	192526.4	16.62	19188	WHT	114516+193245	114516.18	193245.1	16.80	19669	WHT
114310+191519	114310.29	191519.2	17.41	23578	WHT	114517+200120	114517.10	200120.7	15.32	14745	LOI
114313+200747	114313.18	200747.9	16.40	5383	CAN	114517+201108	114517.29	201108.8	18.21	79253	WHT
114314+194821	114314.49	194821.7	19.29	71433	WHT	114517+200110	114517.64	200110.0	15.46	14713	LOI
114314+192534	114314.99	192534.3	15.76	23867	CAN	114520+194220	114520.33	194220.3	20.44	54544	WHT
114317+195525	114317.25	195525.1	18.88	30273	WHT	114520+193259	114520.49	193259.4	17.48	4653	WHT
114317+194658	114317.61	194658.2	15.69	6295	CAN	114522+195146	114522.62	195146.5	21.14	18012	WHT
114318+201523	114318.05	201523.3	17.81	46170	WHT	114524+201239	114524.33	201239.3	18.73	44376	WHT
114319+192520	114319.68	192520.9	15.99	6757	WHT	114526+201056	114526.27	201056.8	16.40	20134	CAN
114320+193637	114320.44	193637.1	19.71	44171	WHT	114529+195658	114529.39	195658.2	16.29	24000	WHT
114320+195206	114320.66	195206.2	18.15	52416	WHT	114530+193639	114530.37	193639.4	17.20	40000	LOI
114322+195704	114322.06	195704.7	16.94	7909	WHT	114531+200217	114531.31	200217.5	19.78	45691	WHT
114324+194121	114324.66	194121.4	18.33	35778	WHT	114533+194505	114533.88	194505.9	18.11	31440	WHT
114332+201326	114332.24	201326.1	16.46	33438	CAN	114533+200028	114533.97	200028.7	17.56	35830	WHT
114332+195108	114332.72	195108.2	19.07	14313	WHT	114536+194253	114536.19	194253.7	18.60	48966	WHT
114335+200005	114335.47	200005.6	16.38	20600	CAN	114540+194302	114540.32	194302.8	17.74	5545	WHT
114336+193930	114336.07	193930.8	19.24	44616	WHT	114543+193854	114543.65	193854.9	16.93	7828	LOI
114337+193835	114337.17	193835.8	17.31	12502	WHT	114543+193905	114543.77	193905.9	16.30	7301	LOI
114337+201533	114337.82	201533.5	20.19	11464	WHT	114544+194013	114544.86	194013.3	17.18	19487	WHT
114339+193446	114339.09	193446.2	16.01	7477	WHT	114545+193151	114545.66	193151.4	18.57	6880	LOI
114342+193636	114342.18	193636.3	19.26	71296	WHT	114545+201200	114545.78	201200.3	19.11	27431	WHT
114343+195607	114343.12	195607.8	18.56	19711	WHT	114548+192708	114548.13	192708.4	16.72	30193	WHT
114345+201252	114345.50	201252.2	19.27	20476	WHT	114549+195915	114549.88	195915.3	15.87	20035	CAN
114350+195702	114350.16	195702.0	17.98	6848	WHT	114550+194824	114550.61	194824.6	18.85	41484	WHT
114350+194138	114350.83	194138.0	19.13	72744	WHT	114602+194754	114602.12	194754.3	19.62	73746	WHT
114353+195004	114353.42	195004.6	19.23	27946	WHT	114605+195151	114605.35	195151.0	18.86	46635	WHT
114353+194422	114353.45	194422.2	15.66	6141	WHT	114620+194518	114620.85	194518.0	17.58	45683	WHT
114353+194315	114353.61	194315.8	17.17	23578	WHT						